THE JOURNAL OF PHYSICAL CHEMISTRY B

Article

pubs.acs.org/JPCB

Structure of $ZnCl_2$ Melt. Part I: Raman Spectroscopy Analysis Driven by Ab Initio Methods

Abduljabar Q. Alsayoud, Manga Venkateswara Rao, Angharad N. Edwards, Pierre A. Deymier, Krishna Muralidharan, B. G. Potter, Jr., Keith Runge, and Pierre Lucas*

Department of Materials Science and Engineering, University of Arizona, Tucson, Arizona 85721, United States

ABSTRACT: The structure of molten $ZnCl_2$ is investigated using a combination of computer simulation and experimental methods. Ab initio molecular dynamics (AIMD) is used to model the structure of $ZnCl_2$ at 600 K. The structure factors and pair distribution functions derived from AIMD show a good match with those previously measured by neutron diffraction (ND). In addition, Raman spectroscopy is used to investigate the structure of liquid $ZnCl_2$ and identify the relative fractions of constituent structural units. To ascertain the assignment of each Raman mode, a series of $ZnCl_2$ crystalline prototypes are modeled and the corresponding Raman modes are derived by first-principles calculations. Curve fitting of experimental Raman spectra using these mode assignments shows excellent agreement with both AIMD and ND. These results confirm the presence of significant fractions of edge-sharing tetrahedra in liquid $ZnCl_2$. The presence of these structural motifs has significant impact on the fragility of this tetrahedral glass-forming liquid. The assignment of Raman bands present in molten $ZnCl_2$ is revised and discussed in view of these results.

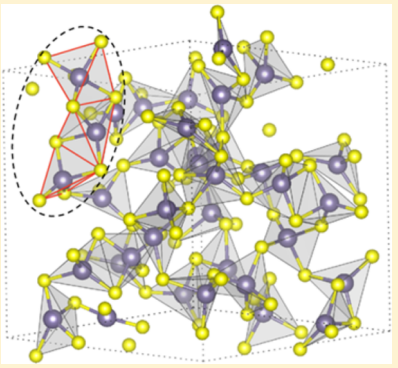

1. INTRODUCTION

The storage of solar energy in the form of heat using high-temperature fluids is a key approach in the development of efficient concentrated solar power plants. In that respect, molten salts have proven to be some of the most attractive media to store and transport thermal energy.[1] In particular, $ZnCl_2$-based salts have recently been the focus of regained interest for this application.[2,3] The key to the performance of these salts is their thermodynamic and transport properties. Understanding and predicting such properties relies on accurate structural information.[4]

Glassy and molten $ZnCl_2$ have been extensively studied because of their unique nature as a prototypical ionic network glass-forming system.[5−15] Unlike other 2−1 salts, $ZnCl_2$ has low conductivity and high viscosity and tends to form glass easily.[16−19] This is usually associated with the persistence of a tetrahedral network structure in the liquid, somewhat reminiscent of silica melts.[6,7,10] The structure of molten $ZnCl_2$ has been studied using multiple techniques including Raman spectroscopy,[7,20−23] neutron diffraction (ND),[8,10,14] and extended X-ray absorption fine structure (EXAFS).[24] All these techniques indeed indicate the predominance of tetrahedra consisting of Zn^{2+} ions surrounded by four Cl^- ions. These $ZnCl_4$ building blocks are then interconnected to form an extended network. However, it was recently suggested using both Raman[7] and ND[10,14] that unlike silica melts (where all tetrahedra are corner-shared) the structure of $ZnCl_2$ contains a significant fraction of edge-shared tetrahedra. These structural features are believed to have important consequences on the dynamical behavior of the molten salt.[13] Hence, a detailed description of the melt structure is valuable, in particular regarding the ratio of edge- and corner-sharing units. The objective of this work is therefore to study the structure of liquid $ZnCl_2$ at 600 K using a combination of ab initio molecular dynamics (AIMD), first-principles calculations, and high-temperature Raman spectroscopy.

Raman spectroscopy is a powerful method to explore the structure of solids and liquids; however, one of its limitations lies in the uncertainty of the peak assignments required for curve-fitting complex spectral features. In this study we therefore use first-principles calculations to determine the Raman-active modes associated with different structural motifs in order to ascertain the validity of the peak assignment. We then curve fit the high-temperature spectra to obtain the fraction of each structural unit in order to characterize short-range order in liquid $ZnCl_2$. Furthermore, we use a density functional theory (DFT)-based AIMD simulation to predict the molten salt structure. The AIMD results are shown to be in excellent agreement with experiment.

2. METHODS

2.1. Computational Methods. *2.1.1. Ab Initio MD of $ZnCl_2$ Melt.* Several classical molecular dynamic simulations of molten $ZnCl_2$ have been previously attempted using a variety of potentials to describe ionic interactions.[25−30] However, these models either failed to reproduce the experimental pair correlation functions or used unrealistic dispersion terms.

Received: March 8, 2016
Revised: April 12, 2016

DOI: 10.1021/acs.jpcb.6b02452
J. Phys. Chem. B XXXX, XXX, XXX−XXX

Therefore, for a more accurate description of the $ZnCl_2$ melt structure, we performed DFT-based AIMD simulations.

AIMD simulations were carried out with the Vienna Ab Initio Simulation Package (VASP)[31,32] using the projector augmented wave (PAW)[33,34] method with the Perdew–Burke–Ernzerhof (PBE)[35] exchange-correlation functional. The Newton equations of motion were calculated by using a Verlet algorithm, as implemented in VASP, with a time-step of 3 fs. A canonical ensemble with a Nose thermostat is used to control the temperature, wherein the Nose mass—i.e., a parameter to control oscillations in the temperature of the ensemble—is estimated using the vibrational frequency of molten $ZnCl_2$.

A cubic simulation cell with randomly placed Zn (36 atoms) and Cl (72 atoms) is initially equilibrated at 2000 K for 6 ps and is subsequently quenched to 600 K, using a quench rate of 1.8×10^{14} K/s. The equilibrium volume of the cell corresponding to zero pressure at 600 K is obtained from a series of five high-accuracy calculations, employing a plane wave cutoff energy of 560 eV and a Monkhorst–Pack k-mesh of $2 \times 2 \times 2$ size. A final run to predict the liquid structure of $ZnCl_2$ at the obtained equilibrium volume is carried out for 17.88 ps. On the basis of a series of runs performed at 9.88 and 12.88 ps, the 17.88 ps duration in AIMD was found to be long enough to reach convergence, and the populations of various structural features such as tetrahedral units, and their corner or edge sharing, were found to be converged within ±1.1%. All the runs, except the high-accuracy runs to predict the equilibrium volume, were carried out using a plane wave cutoff energy of 280 eV and with a Gamma point k-mesh of $1 \times 1 \times 1$. The structural analysis of $ZnCl_2$ liquids is performed by using the R.I.N.G.S. code.[36]

2.1.2. First-Principles Calculation of Raman Modes. If the structure of the $ZnCl_2$ melt is considered to be composed entirely of $ZnCl_4$ tetrahedral units, only three distinct types of Zn local structural environments can be identified as depicted in Figure 1. The environments denoted $Zn^{(0)}$, $Zn^{(1)}$, and $Zn^{(2)}$

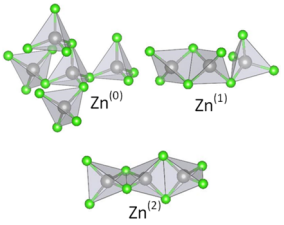

Figure 1. Local environment of Zn atoms in liquid $ZnCl_2$.

represent a tetrahedron that shares all corners but no edges, shares one edge, and shares two edges with other tetrahedra, respectively.[14]

To calculate the Raman mode for each of these environments, three tetrahedrally connected solid structural models were chosen to model the three types of connectivity. The structure types are δ-$ZnCl_2$ ($Pna2_1$),[37] $BeCl_2$ (*Ibam*),[38] and GeS_2 ($P12_1/c1$)[39] as depicted on Figure 2. The δ-$ZnCl_2$ structure consists of only corner-sharing tetrahedra and hence represents $Zn^{(0)}$. The $BeCl_2$-type structure has only edge-sharing tetrahedral units and is used to model $Zn^{(2)}$. The GeS_2-type structure is a prototype of mixed corner- and edge-sharing tetrahedra that contains 50% $Zn^{(0)}$ and 50% $Zn^{(1)}$ units. For the Raman mode calculation, the δ-$ZnCl_2$ structure was used "as is" but the hypothetical $ZnCl_2$ structures corresponding to $BeCl_2$ and GeS_2 were modeled by first-principles calculation. Zn was

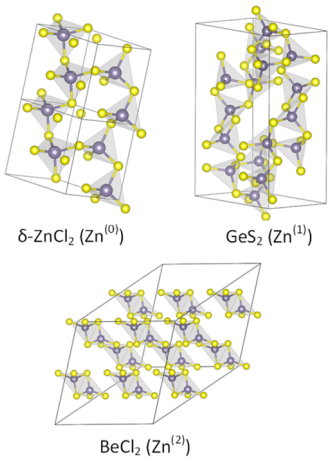

Figure 2. Crystalline prototypes used to model the Raman modes of structural units present in $ZnCl_2$ liquid.

substituted for Be and Ge in $BeCl_2$ and GeS_2, respectively, and Cl was substituted for S in GeS_2. The volume of the $BeCl_2$- and GeS_2-type unit cells was then altered such that the Zn–Cl distance was the same as the one in δ-$ZnCl_2$. Another correction method was used to adjust the volume based on δ-$ZnCl_2$ density; however, density correction resulted in Zn–Cl shrinkage that was not physical for some structures.

For the Raman mode calculation, density functional theory (DFT) calculations were implemented within the plane-wave based CASTEP[40] code. Phonons and Raman activities were calculated using the density-functional perturbation theory method (DFPT).[41] Ion-valence electron interaction was described using norm-conserving pseudopotentials,[42] as these are the only pseudopotentials adopted for DFPT calculation in CASTEP. To achieve high accuracy, generalized gradient approximation (GGA)-PBE was used to describe correlation and exchange potentials. All calculations were performed with a 700 eV energy cutoff. Geometry optimization of the structures was done using several convergence parameters. The first one is that the change in total energy was $<10^{-6}$ eV/atom. Other convergence parameters include a force per atom smaller than 10^{-3} eV/Å and a maximum displacement of atoms less than 10^{-3} Å. Phonon calculations were conducted with the same accuracy as the geometry optimization, and Raman calculations were done at the gamma point ($q = 0$). Primitive unit cells were used for all the structures. The k-mesh for each structure was chosen to get the same level of accuracy: $2 \times 2 \times 2$ for δ-$ZnCl_2$, $2 \times 2 \times 4$ for $BeCl_2$, and $1 \times 1 \times 2$ for GeS_2.

2.1.3. Convergence Test. A convergence test was also performed in order to ensure total energy and phonon convergence as a function of both cutoff energy and k-mesh. First, single-point energy was calculated at 400 eV with k-mesh ranging from $2 \times 2 \times 2$ to $16 \times 16 \times 16$. The difference in energy between $2 \times 2 \times 2$ and $16 \times 16 \times 16$ was 1.76 meV per atom, indicating good convergence for $2 \times 2 \times 2$. Then, the energy convergence for $2 \times 2 \times 2$ at different cutoff energies was also done where the difference between 700 and 900 eV was 31.86 meV per atom. This is quite a large difference, but we used 700 eV in our calculations due to CPU limitation and because its effect on phonon density of states (PDOS) is not so large.

The phonon convergence test was done as a function of both k-mesh and cutoff energy. First, phonon convergence at 700 eV with k-mesh ranging from $2 \times 2 \times 2$ to $4 \times 2 \times 4$ was

DOI: 10.1021/acs.jpcb.6b02452
J. Phys. Chem. B XXXX, XXX, XXX–XXX

performed and phonon convergence was evaluated by the difference between the major peaks as well as the highest-frequency phonon positions. The difference between the 2 × 2 × 2 and 4 × 2 × 4 was ~1.5 cm^{-1}. Then phonon convergence was performed for 2 × 2 × 2 from 700 to 900 eV. The frequency difference between 700 and 900 eV was <2.5 cm^{-1}, which validates the use of 700 eV in our calculations. Hence, the propagation of these two errors yields a total error bar on Raman spectra of 2.9 cm^{-1}.

2.2. Experimental Method. Anhydrous $ZnCl_2$ (99.999% purity) was purchased from Alfa Aesar and stored in a glovebox under an argon atmosphere with <0.1 ppm of H_2O and O_2 concentrations. The crystal structure of the sample was confirmed to be δ-$ZnCl_2$ using X-ray diffraction performed in a quartz capillary sealed under argon to prevent contact with moisture. The melting point of high-purity $ZnCl_2$ was found to be 588 K using differential scanning calorimetry.

Raman measurements were collected using a Jobin-Yvon Horiba Lab Ram HR800 spectrometer with an inverted microscope. The spectra were collected using an argon ion laser (λ_{ex} = 514.5 nm) in a backscattering configuration using a long working distance 10× objective (WD = 35 mm, NA = 0.28) and 1800 g/mm grating to give a beam spot size of 100 μm. The power of the laser was 100 mW. The spectra integration time was 4 min, and an average of two spectra were collected. The Raman shift was measured from 0 to 800 cm^{-1}. This range emcompasses the anticipated Raman signal of liquid $ZnCl_2$, which extends up to <500 cm^{-1}.

A custom-made heating stage was used for measuring Raman spectra of liquids up to 400 °C. It consisted of a heating block fitted with four symmetrically positioned heating cartridges for homogeneous heat distribution and a thermocouple for temperature control. The samples (4 g) were sealed in a glass vial (outer diameter was 16 mm with 2 mm thick walls) under vacuum and inserted in a tight-fitted cylindrical opening along the vertical length of the heating block. The Raman signal was then collected through the 2-mm-thick flat bottom of the vial with optical access afforded by a hole at the bottom of the heating block. The laser beam was first focused on the bottom of the glass vial (as confirmed by observation of the characteristic glass Raman spectrum). Repositioning of the objective allowed the focus to then be moved an estimated 2−3 mm into the melt volume. The final focus position was optimized by maximizing the δ-$ZnCl_2$ Raman spectrum intensity. The sample was allowed to equilibrate for 45 min before taking the measurement. All Raman spectra were baseline corrected and thermally reduced to account for the temperature dependence of the scattering intensity.

3. RESULTS

3.1. Computational. *3.1.1. Ab Initio MD of $ZnCl_2$ Melt at 600 K.* Figure 3 presents the total structure factor and partial structure factors S_{Cl-Cl}, S_{Zn-Zn}, and S_{Zn-Cl} calculated from the AIMD simulations of $ZnCl_2$ at 600 ± 45 K. The structure factors are obtained from the Fourier transform of the radial distribution functions. The structure factor in the low-q range reveals the short-range order in these network-forming liquids. To assess the validity of the AIMD structural predictions, the structure factors are compared with experimental neutron diffraction data obtained by the isotopic substitution method and reverse Monte Carlo (RMC) modeling from Zeidler et al.[10] These results indicate that the features of the theoretical

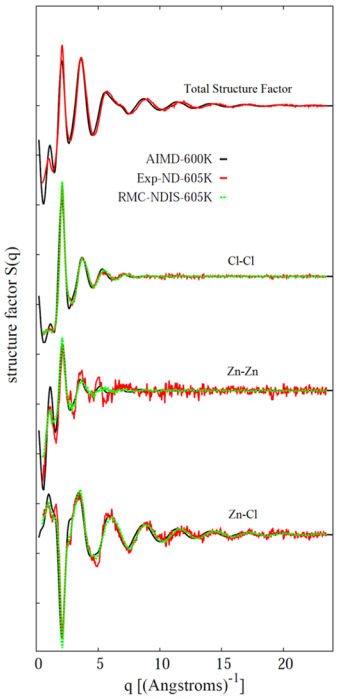

Figure 3. Total and partial structure factors (Zn−Cl, Zn−Zn, and Cl−Cl) calculated from AIMD (black solid) and compared with experimental ND results from Zeidler et al.[10] (red line) and the corresponding RMC model (green dash).

structure factors are in good agreement with the experimental data.

The partial pair distributions for Zn−Cl, Cl−Cl, and Zn−Zn are also in good agreement with those derived from experimental ND (Figure 4). In particular the first peak of

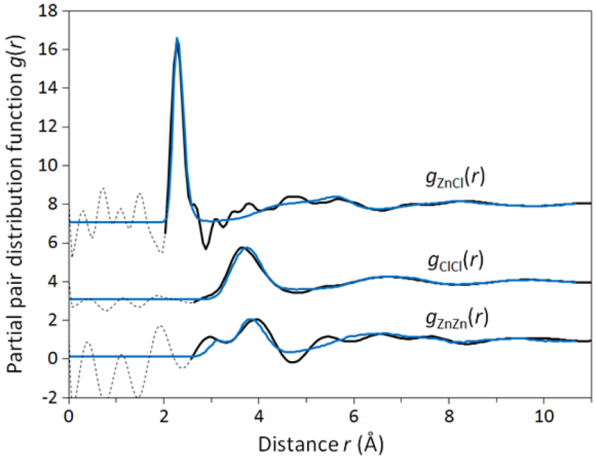

Figure 4. Partial pair-distribution function for Zn−Cl, Cl−Cl, and Zn−Zn calculated by AIMD (blue curve) and ND results from Zeidler at al.[10] obtained by Fourier transform of the structure factors of Figure 3.

$g_{ZnCl}(r)$ at r_{ZnCl} = 2.27 Å is consistent with the expected Zn−Cl bond distance in a $ZnCl_4$ tetrahedron.[37] Interestingly the Zn−Zn pair correlation $g_{ZnZn}(r)$ exhibits two peaks centered near 3.1 and 3.8 Å that are also present in the ND. Considering a Zn−Cl bond distance of 2.27 Å, the 3.8 Å peak is in agreement with the Zn−Zn distance expected between the central Zn ions in two adjacent corner-sharing tetrahedra while the 3.1 Å peak

DOI: 10.1021/acs.jpcb.6b02452
J. Phys. Chem. B XXXX, XXX, XXX−XXX

is consistent with the Zn−Zn distance expected between the central Zn ions in two adjacent edge-sharing tetrahedra.[10] Furthermore, these peak assignments are consistent with the Zn−Zn distances for edge- and corner-sharing tetrahera derived from the crystalline prototype depicted in Figure 2, as will be discussed in section 3.1.2.

This structural interpretation is further supported by the bond angle distribution for Zn−Cl−Zn shown in Figure 5. The

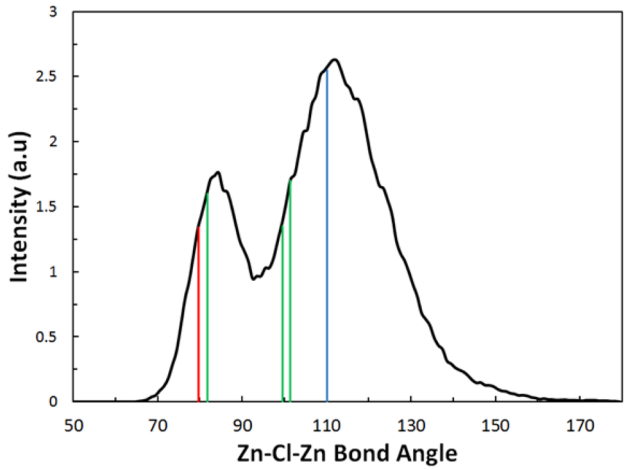

Figure 5. Bond angle distribution for Zn−Cl−Zn calculated from AIMD. The lines correspond to the bond angles calculated for the structure prototypes δ-$ZnCl_2$ (blue), GeS_2 (green), and $BeCl_2$ (red).

bond angle shows a dual distribution centered near 84° and 112°. Considering a Zn−Cl distance of 2.27 Å, a Zn−Cl−Zn bond angle of 112° would result in a Zn−Zn distance of 3.76 Å, which corresponds to the corner-sharing tertahedra peak observed in $g_{ZnZn}(r)$ at 3.8 Å. Similarly, the Zn−Cl−Zn bond angle of 84° would result in a Zn−Zn distance of 3.05 Å, which relates to the edge-sharing tetrahedra peak observed in $g_{ZnZn}(r)$ at 3.1 Å. These bond angle assignments are also consistent with those for edge- and corner-sharing tetrahedra derived from the crystalline prototype depicted in Figure 2, as will be discussed in section 3.1.2.

Overall, the good match between the experimental and calculated structure factors and pair distribution functions lends credence to the structure derived from AIMD for $ZnCl_2$. The presence of both corner- and edge-sharing tetrahedra is also consistent with other models for liquid $ZnCl_2$.[15,43] To visualize the structural motifs present in the network, a snapshot of the 108-atom model is plotted in Figure 6. This structure reveals the three different types of connectivity predicted in Figure 1, namely, $Zn^{(0)}$, $Zn^{(1)}$, and $Zn^{(2)}$. In addition to these tetrahedral connectivities, we also observe a minor concentration of 3- and 5-fold coordinated Zn. The fractions of each type of connectivity at 600 K were as follows: 57(±7)% $Zn^{(0)}$, 32(±6)% $Zn^{(1)}$, 6(±2)% $Zn^{(2)}$, 3(±3)% 3-fold, and 2(±2)% 5-fold.

3.1.2. Crystal Prototypes and First-Principles Calculation of Raman Modes. The three structure types depicted in Figure 2 were used to gain insight on the three different Zn environments, $Zn^{(0)}$ (δ-$ZnCl_2$), $Zn^{(1)}$ (GeS_2), and $Zn^{(2)}$ ($BeCl_2$). While the δ-$ZnCl_2$ structure was used "as is", the hypothetical $ZnCl_2$ structures corresponding to GeS_2 and $BeCl_2$ were modeled as described in section 2.1.2. In particular these structure prototypes were used to calculate Raman modes, Zn−

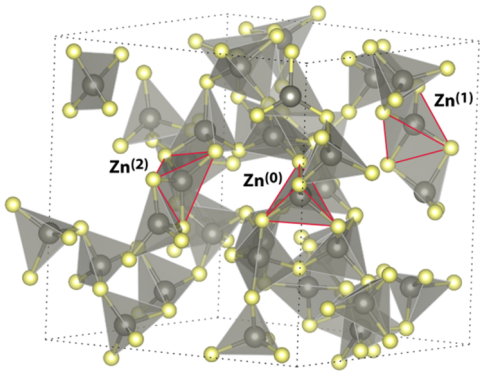

Figure 6. Snapshot of the liquid $ZnCl_2$ at 600 K obtained by AIMD. The unit cell containing 108 atoms reveals the presence of the three different local Zn environments: $Zn^{(0)}$, $Zn^{(1)}$, and $Zn^{(2)}$.

Zn distances, and bond angle distributions for each environment.

As illustrated in Figure 5, the Zn−Cl−Zn bond angles derived from these structure prototypes are consistent with those found by AIMD simulations of the $ZnCl_2$ liquid structure. δ-$ZnCl_2$ has a single Zn−Cl−Zn bond angle of 110° corresponding to a pair of corner-sharing tetrahedra, while $BeCl_2$ has a single bond angle at 80° corresponding to a pair of edge-sharing tetrahedra. GeS_2 instead has two corner-sharing tetrahedra angles near 100° and one edge-sharing tetrahedra angle at 82°. These Zn−Cl−Zn bond angles are consistent with the two bond angle distribution peaks centered at 84° and 112° that are assigned to edge- and corner-sharing tetrahedra, respectively (Figure 5).

Similarly, the Zn−Zn bond distances derived from the structure prototypes are consistent with those derived from the partial pair distribution function calculated by AIMD. Figure 7

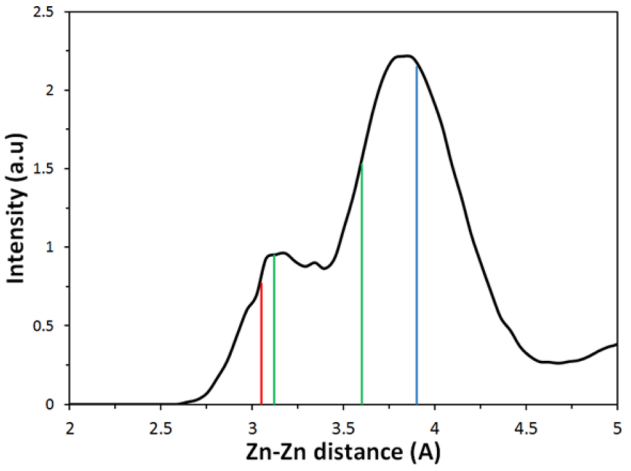

Figure 7. Close-up of the pair-distribution function for Zn−Zn calculated by AIMD. The lines correspond to the Zn−Zn distances calculated for the structure prototypes δ-$ZnCl_2$ (blue), GeS_2 (green), and $BeCl_2$ (red).

shows an enlarged view of the Zn−Zn pair distribution function $g_{ZnZn}(r)$ along with the Zn−Zn bond distances for each structure prototype. Again the pair distribution function shows two peaks centered at 3.8 and 3.1 Å assigned to corner- and edge-sharing tetrahedra, respectively, which are consistent with the Zn−Zn distances for corner-sharing tetrahedra of 3.85 and 3.6 Å found in δ-$ZnCl_2$ and GeS_2, respectively, as well as the

DOI: 10.1021/acs.jpcb.6b02452
J. Phys. Chem. B XXXX, XXX, XXX−XXX

Zn−Zn distances for edge-sharing tetrahedra of 3.06 and 3.11 Å found in $BeCl_2$ and GeS_2, respectively.

Raman modes were then calculated by DFPT for each crystal prototype. Figure 8 shows the position and normalized intensity of all Raman modes for each structure type. The most intense modes for each structure were selected for further comparison with experimental spectra, and a vector analysis was performed to determine their symmetry.

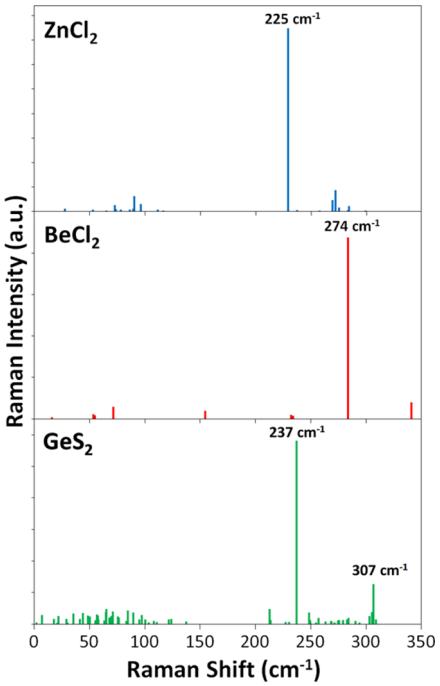

Figure 8. Position and normalized intensity of Raman modes for the structure prototypes δ-$ZnCl_2$ (blue), GeS_2 (green), and $BeCl_2$ (red).

Figure 9 shows that the most intense Raman mode of δ-$ZnCl_2$ at 225 cm^{-1} corresponds to a bending vibration of two corner-sharing tetrahedra. The most intense mode of $BeCl_2$ at 274 cm^{-1} corresponds to an edge-stretching vibration of two edge-sharing tetrahedra. The two modes of GeS_2 at 237 and 307 cm^{-1} show major contributions from the bending vibration of corner-sharing tetrahedra and edge-stretching vibration of edge-sharing tetrahedra, respectively.

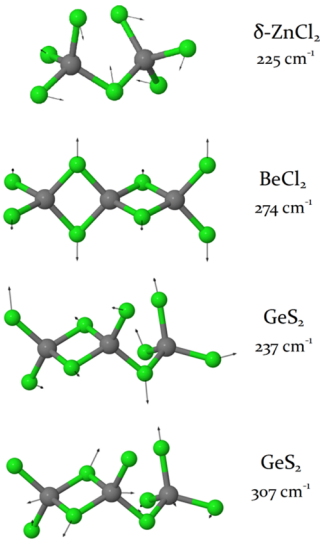

Figure 9. Vector analysis of the main Raman modes for the three structure prototypes.

3.2. Raman Spectroscopy. Raman spectra were acquired for both δ-$ZnCl_2$ at room temperature and liquid $ZnCl_2$ at 600 K as depicted in Figure 10. The main Raman mode around 230 cm^{-1} broadens considerably in the liquid state as previously observed.[6,7] In addition, a sideband around 310 cm^{-1} becomes clearly visible as pointed out by Yannopoulos et al.[7] As expected for a crystalline solid, the main band of δ-$ZnCl_2$ is very sharp. This line is centered at 227 cm^{-1}, which is in good agreement with the value of 225 cm^{-1} found by first-principles calculation for δ-$ZnCl_2$ (Figure 10). This good match substantiates the validity of the DFPT method for calculating reliable Raman shifts.

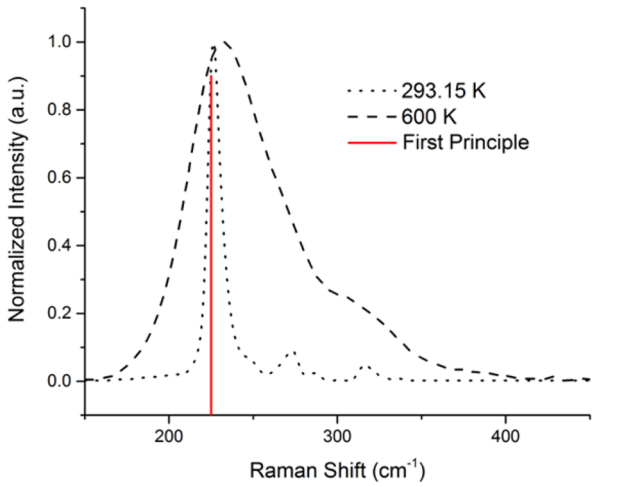

Figure 10. Raman spectrum of δ-$ZnCl_2$ at room temperature and liquid $ZnCl_2$ at 600 K. The line indicates the position of the main Raman mode predicted by first-principles calculations for δ-$ZnCl_2$.

4. DISCUSSION

4.1. Comparison of Experimental and Computational Results. To perform a quantitative comparison of the structural model obtained by AIMD with that derived from Raman spectroscopy, the Raman spectrum collected at 600 K was analyzed using the mode assignment calculated by first principles using CASTEP in Figure 8. After background removal and thermal reduction, curve fitting of the resulting spectrum was pursued, involving the use of Gaussian peaks whose center frequencies were associated with the primary vibrational resonances derived from the DFPT analysis. Goodness of fit was determined by examination of the residual error between the experimental and multi-Gaussian envelope function. Four major peaks were used in the fit, as dictated by the DFPT results (Figure 8). These included the corner-sharing δ-$ZnCl_2$ mode (peak 1) at 225 cm^{-1}, the edge-sharing $BeCl_2$-type mode (peak 2) at 274 cm^{-1}, and the two GeS2-type modes, one corner-sharing (peak 3) at 237 cm^{-1} and one edge-sharing (peak 4) at 307 cm^{-1}. Peak number designations are also provided in Figure 11. An additional peak centered near ~350 cm^{-1} was also used to account for the small fraction of nontetrahedral Zn that arises from broken Cl bridges at higher temperature (peak 5). This assignment was made based on that suggested by Yannopoulos et al.[7] The fraction of these 3-

DOI: 10.1021/acs.jpcb.6b02452
J. Phys. Chem. B XXXX, XXX, XXX−XXX

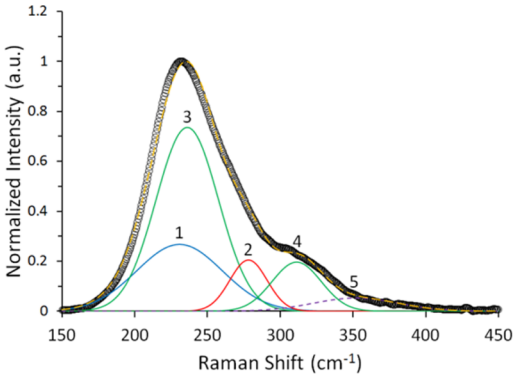

Figure 11. Curve-fitting of the $ZnCl_2$ Raman spectra at 600 K using the Raman modes calculated by first principles in Figure 8. Curve numbering is detailed in the text.

coordinated Zn is estimated at ~3% from AIMD. During the fitting process, the peak positions were allowed to vary by ±5 cm^{-1} in order to optimize agreement with the experimental spectrum. Peak widths were allowed to vary but not exceed the width of peak 1 (δ-$ZnCl_2$). In addition, the ratio of peak 3 to peak 4 (GeS_2-type) was fixed at the same ratio as that calculated in Figure 8. The result of this curve fitting is shown in Figure 11. The R^2 value for the fit in Figure 11 is 0.9979.

The percentage areas of each peak are given in Table 1. The percentage of δ-$ZnCl_2$ is equal to 25%. GeS_2 percentage is equal to 62% (peak 3 + peak 4). Finally, $BeCl_2$ is 11%, and $ZnCl_3$ is 5%. Peak areas were largely insensitive to changes in starting peak position parameters. These percentages can then be used to estimate the relative abundance of each Zn local environment. Peak 1 (δ-$ZnCl_2$) corresponds to pure $Zn^{(0)}$, while peak 2 ($BeCl_2$) corresponds to pure $Zn^{(2)}$. The percentages corresponding to the GeS_2-type modes were quantified as follows. The unit cell of the GeS_2 prototype crystal (Figure 2) contains as many $Zn^{(0)}$ as $Zn^{(1)}$; hence, the total intensity of peak 3 + peak 4 divided by 2 was used to quantify the fraction of each Zn type. This treatment requires that the structure contains a roughly equal number of $Zn^{(1)}$ and $Zn^{(0)}$ of the GeS_2-type. This requirement is found to be satisfied a posteriori by compiling the fraction of various Zn environments found in the 108-atom AIMD model. This calculation requires differentiating each Zn environment based on their first Zn neighbors. For example, a $Zn^{(0)}$ can share corners with all $Zn^{(0)}$, all $Zn^{(1)}$, or a combination of the two. Here we consider that $Zn^{(0)}$ sharing corners with 3 or 4 other $Zn^{(0)}$ are similar and are assigned to peak 1. Similarly, $Zn^{(0)}$ sharing corners with 2 or more $Zn^{(1)}$ are close to the GeS_2-type motif and are assigned to peak 3. Then all $Zn^{(1)}$ are assigned to the GeS_2-type peak 4 and all $Zn^{(2)}$ are assigned to the $BeCl_2$-type peak 2.

Table 1. Percentage Area of the Five Raman Peaks Resulting from the Curve Fitting Shown in Figure 11 (Uncertainties Calculated from Multiple Curve-Fitting Attempts Were <1%)

	% area
peak 1	25%
peak 2	8%
peak 3	51%
peak 4	11%
peak 5	5%

Hence, the percentage of each Zn environment is calculated as follow:

$$\%Zn^{(0)} = \%peak1 + \%(0.5 \times peak3 + 0.5 \times peak4)$$

$$\%Zn^{(1)} = \%(0.5 \times peak3 + 0.5 \times peak4)$$

$$\%Zn^{(2)} = \%peak3$$

The results of this calculation are reported in Table 2. It must be mentioned that the small fraction of 3-coordinated Zn was ignored in the calculation of the Raman and AIMD ratios in order to compare with the ND data reported by Zeidler at al.[14] Overall the results of Table 2 indicate a good quantitative agreement between ND, Raman, and AIMD. This further supports the validity of the structure derived by AIMD.

Table 2. Comparison of the Relative Fraction of $Zn^{(0)}$, $Zn^{(1)}$, and $Zn^{(2)}$ Derived by Raman, AIMD, and ND (From Zeidler et al.[14])

	Raman	AIMD	ND
$Zn^{(0)}$	59%	60%	60%
$Zn^{(1)}$	32%	34%	30%
$Zn^{(2)}$	9%	6%	10%

4.2. Assignment of Raman Bands in Liquid $ZnCl_2$. The assignment of the main Raman band in tetrahedral MX_2 systems has been interpreted in various ways.[44] Bell and Dean initially assigned the main Raman mode to a rocking motion of the X atom perpendicular to the X−M−X plane.[44] However, Galeener later interpreted it as the symmetric stretch of the X atom along a line bisecting the X−M−X angle.[45] For $ZnCl_2$ this main mode has been broadly interpreted as a "totally symmetric stretching mode" of $ZnCl_4$ tetrahedra[22,23,46] or specifically as an A_1 breathing mode.[7] In that respect the vector analysis of δ-$ZnCl_2$ shown in Figure 9 indicates that the main mode at 225 cm^{-1} is associated with a motion of the Cl atom perpendicular to the Zn−Cl−Zn plane. This assignment is in good agreement with that initially proposed by Bell and Dean for MX_2 tetrahedral systems.[44] This divergence in assignment most likely arises from the fact that many studies commonly use the factor group analysis to interpret the Raman modes of crystalline $ZnCl_2$.[6,7] However, this analysis treats structural units as individual molecules in order to assign point group symmetries and to derive atomic motions.[47] While this is an adequate approach for treating molecular solids, it would appear to be inadequate for solids showing strong network character such as $ZnCl_2$. Overall our results agree well with those of Bell and Dean, which were indeed derived from an extended three-dimensional model of silica.[44] Nevertheless, while the exact symmetry of the main Raman mode at 225 cm^{-1} may be debated, there is no question that it is associated with the vibration of corner-sharing tetrahedra, and therefore it can reliably be used as a mean of quantifying the relative abundance of this type of structural unit.

The first-principles calculations of Figure 8 and the vector analysis of Figure 9 also suggest some new assignments for Raman bands present in molten $ZnCl_2$. The shoulder peaks arising near ~275 and ~300 cm^{-1} at high temperature have initially been associated with an increasing concentration of broken −Cl− bridges in the $ZnCl_2$ network.[20,22,46] Irish and Young suggested the formation of individual $ZnCl_2$, $ZnCl_3^-$, and $ZnCl_4^{2-}$ units,[20] while later studies assigned these modes to

DOI: 10.1021/acs.jpcb.6b02452
J. Phys. Chem. B XXXX, XXX, XXX−XXX

nonbridging Cl[22,46] on the basis of the "split cell model" of Angell and Wong.[6] Cacciola et al. instead assigned these bands to a LO−TO splitting of the antisymmetric tetrahedral stretching mode.[23] Yannopoulos et al. were the first to suggest that the shoulder near ∼300 cm^{-1} could instead be associated with $BeCl_2$-type strips of edge-sharing tetrahedra.[7] They describe the melt structure as a mixture of chains of edge-sharing tetrahedra and clusters of corner-sharing tetrahedra. Our results support the presence of edge-sharing tetrahedra but only in small chain fragments of 2−3 units, which are in turn fully integrated within the continuous network structure of the melt. This model requires the presence of a significant fraction of $Zn^{(1)}$ to link edge- and corner-sharing tetrahedra. We therefore suggest that two modes associated with edge-sharing tetrahedra are present, one $BeCl_2$-type mode ($Zn^{(2)}$) near 274 cm^{-1} and one GeS2-type mode ($Zn^{(1)}$) near 306 cm^{-1}. The existence of significant concentrations of these edge-sharing tetrahedra in molten $ZnCl_2$ has since been unambiguously demonstrated by ND.[10,14] The present AIMD calculation also corroborates their existence. This further reinforces the validity of these Raman mode assignments.

4.3. Edge-Sharing Tetrahedra in Liquid $ZnCl_2$. The existence of edge-sharing units in tetrahedral network liquids is of significant importance as it appears to be affecting the transport properties of the melts. Indeed, molecular dynamic simulations of MX_2 tetrahedral liquids have shown that the melt fragility increases with the number of edge-sharing motifs.[13] These predictions are also consistent with the temperature-dependent constraint model of Gupta and Mauro,[48] which correlates the number of topological degrees of freedom to the melt fragility. Indeed, a pair of edge-sharing tetrahedra generates 12 angular constraints compared to 14 for a pair of corner-sharing tetrahedra;[49] hence, an increasing fraction of edge-sharing tetrahedra will result in more structural degrees of freedom and consequently will lead to increased fragility. An investigation of the temperature dependence of edge-sharing tetrahedra concentration would therefore be of much interest and will be the subject of a future study.

5. CONCLUSIONS

In this paper, the structure of liquid $ZnCl_2$ at 600 K was investigated using a combination of experimental and ab initio numerical methods. Liquid structure information derived from AIMD was used to investigate short-range ordering. This structural information is shown to be in good agreement with isotopically substituted ND data previously published by Zeidler et al.[10] and suggests the presence of both corner- and edge-sharing tetrahedra in the melt. The AIMD model was further validated by Raman spectroscopy. First, the Raman mode assignments were derived from three simulated prototypical structures for $ZnCl_2$ using CASTEP and employed for the curve fitting of experimental spectra. This approach led to an excellent agreement between the fractions of structural motifs obtained by Raman, ND, and AIMD. The structure of liquid $ZnCl_2$ at 600 K was shown to be composed of a three-dimensional network of corner-sharing tetrahedra with a homogeneously distributed fraction of edge-sharing tetrahedra. Having such understanding of the structure and its evolution as a function of temperature will enable better prediction of thermal and transport properties such as the melt fragility. In the case of zinc chloride, this information is crucial in predicting and designing thermal and transport properties of $ZnCl_2$-based heat transfer fluids.

AUTHOR INFORMATION

Corresponding Author

*E-mail: pierre@u.arizona.edu. Tel.: 1-520-322-2311.

Notes

The authors declare no competing financial interest.

ACKNOWLEDGMENTS

We are very grateful to Philip Salmon and Anita Zeidler for providing the neutron diffraction data of Figure 4. This project was supported by DOE-MURI Grant no. DE-EE0005942 under the U.S. DoE Sunshot program. A.Q.A. acknowledges King Fahad University of Petroleum and Minerals (KFUPM) for their financial support during his Ph.D.

REFERENCES

(1) Raade, J. W.; Padowitz, D. Development of Molten Salt Heat Transfer Fluid With Low Melting Point and High Thermal Stability. *J. Sol. Energy Eng.* **2011**, *133* (3), 031013.

(2) Vignarooban, K.; Xu, X.; Wang, K.; Molina, E. E.; Li, P.; Gervasio, D.; Kannan, A. M. Vapor pressure and corrosivity of ternary metal-chloride molten-salt based heat transfer fluids for use in concentrating solar power systems. *Appl. Energy* **2015**, *159*, 206−213.

(3) Manga, V. R.; Bringuier, S.; Paul, J.; Jayaraman, S.; Lucas, P.; Deymier, P.; Muralidharan, K. Molecular dynamics simulations and thermodynamic modeling of NaCl-KCl-ZnCl2 ternary system. *CALPHAD: Comput. Coupling Phase Diagrams Thermochem.* **2014**, *46*, 176−183.

(4) Manga, V. R.; Swinteck, N.; Bringuier, S.; Lucas, P.; Deymier, P.; Muralidharan, K. Interplay between structure and transport properties of molten salt mixtures of $ZnCl_2$−NaCl−KCl: A molecular dynamics study. *J. Chem. Phys.* **2016**, *144* (9), 094501.

(5) Salmon, P. S.; Martin, R. A.; Mason, P. E.; Cuello, G. J. Topological versus chemical ordering in network glasses at intermediate and extended length scales. *Nature* **2005**, *435* (7038), 75−78.

(6) Angell, C. A.; Wong, J. Structure and glass transition thermodynamics of liquid zinc chloride from far-infrared, Raman, and probe ion electronic and vibrational spectra. *J. Chem. Phys.* **1970**, *53* (5), 2053−2066.

(7) Yannopoulos, S. N.; Kalampounias, A. G.; Chrissanthopoulos, A.; Papatheodorou, G. N. Temperature induced changes on the structure and the dynamics of the "tetrahedral" glasses and melts of ZnCl2 and ZnBr2. *J. Chem. Phys.* **2003**, *118* (7), 3197−3214.

(8) Biggin, S.; Enderby, J. E. The structure of molten zinc chloride. *J. Phys. C: Solid State Phys.* **1981**, *14* (22), 3129−36.

(9) Angell, C. A.; Williams, E.; Rao, K. J.; Tucker, J. C. Heat capacity and glass transition thermodynamics for zinc chloride. A failure of the first Davies-Jones relation for dTg/dP. *J. Phys. Chem.* **1977**, *81* (3), 238−43.

(10) Zeidler, A.; Salmon, P. S.; Martin, R. A.; Usuki, T.; Mason, P. E.; Cuello, G. J.; Kohara, S.; Fischer, H. E. Structure of liquid and glassy ZnCl2. *Phys. Rev. B: Condens. Matter Mater. Phys.* **2010**, *82* (10), 104208.

(11) Wilson, M.; Madden, P. A. Voids, Layers, and the First Sharp Diffraction Peak in ZnCl2. *Phys. Rev. Lett.* **1998**, *80* (3), 532−535.

(12) Sharma, B. K.; Wilson, M. Intermediate-range order in molten network-forming systems. *Phys. Rev. B: Condens. Matter Mater. Phys.* **2006**, *73* (6), 060201.

(13) Wilson, M.; Salmon, P. S. Network topology and the fragility of tetrahedral glass-forming liquids. *Phys. Rev. Lett.* **2009**, *103* (15), 157801.

(14) Zeidler, A.; Chirawatkul, P.; Salmon, P. S.; Usuki, T.; Kohara, S.; Fischer, H. E.; Howells, W. S. Structure of the network glass-former ZnCl2: From the boiling point to the glass. *J. Non-Cryst. Solids* **2015**, *407*, 235−245.

DOI: 10.1021/acs.jpcb.6b02452
J. Phys. Chem. B XXXX, XXX, XXX−XXX

(15) Bassen, A.; Lemke, A.; Bertagnolli, H. Monte Carlo and reverse Monte Carlo simulations on molten zinc chloride. *Phys. Chem. Chem. Phys.* **2000**, *2* (7), 1445−1454.
(16) Mackenzie, J. D.; Murphy, W. K. Structure of glass-forming halides. II. Liquid zinc chloride. *J. Chem. Phys.* **1960**, *33*, 366−9.
(17) Gruber, G. J.; Litovitz, T. A. Shear and structural relaxation in molten zinc chloride. *J. Chem. Phys.* **1964**, *40* (1), 13−26.
(18) Easteal, A. J.; Angell, C. A. Viscosity of Molten ZnCl2 and Supercritical Behavior in Its Binary Solutions. *J. Chem. Phys.* **1972**, *56* (8), 4231−4233.
(19) Susic, M. V.; Mentus, S. V. Viscosity and structure of molten zinc chloride and zinc bromide. *J. Chem. Phys.* **1975**, *62* (2), 744.
(20) Irish, D. E.; Young, T. F. Raman spectrum of molten zinc chloride. *J. Chem. Phys.* **1965**, *43* (5), 1765−67.
(21) Polsky, C. H.; Martinez, L. M.; Leinenweber, K.; VerHelst, M. A.; Angell, C. A.; Wolf, G. H. Pressure-induced crystallization of vitreous ZnCl2. *Phys. Rev. B: Condens. Matter Mater. Phys.* **2000**, *61* (9), 5934−5938.
(22) Aliotta, F.; Maisano, G.; Migliardo, P.; Vasi, C.; Wanderlingh, F.; Smith, G. P.; Triolo, R. Vibrational dynamics of glassy and molten zinc chloride. *J. Chem. Phys.* **1981**, *75* (2), 613.
(23) Cacciola, M. L.; Magazu, S.; Migliardo, P.; Aliotta, F.; Vasi, C. Some evidence of LO-TO splitting in disordered zinc dichloride. *Solid State Commun.* **1986**, *57* (7), 513−17.
(24) Hefeng, L.; Kunquan, L.; Zhonghua, W.; Jun, D. EXAFS studies of molten ZnCl2, RbCl and Rb2ZnCl4. *J. Phys.: Condens. Matter* **1994**, *6* (20), 3629−40.
(25) Woodcock, L. V.; Angell, C. A.; Cheeseman, P. Molecular dynamics studies of the vitreous state: Simple ionic systems and silica. *J. Chem. Phys.* **1976**, *65* (4), 1565.
(26) Gardner, P. J.; Heyes, D. M. Molecular dynamics computer simulations of molten zinc chloride. *Physica B+C (Amsterdam)* **1985**, *131* (1−3), 227−233.
(27) Ballone, P.; Pastore, G.; Thakur, J. S.; Tosi, M. P. Pair structure and interionic forces in molten zinc chloride. *Physica B+C (Amsterdam)* **1986**, *142* (3), 294−300.
(28) Abramo, M. C.; Pizzimenti, G. Models and structure predictions in computer simulation of molten zinc chloride. *Phys. B (Amsterdam, Neth.)* **1989**, *154* (2), 203−8.
(29) Kumta, P. N.; Deymier, P. A.; Risbud, S. H. Improved rigid ion model of molten zinc chloride. *Phys. B (Amsterdam, Neth.)* **1988**, *153* (1−3), 85−92.
(30) Wilson, M.; Madden, P. A. Short- and intermediate-range order in metal chloride (MCl2) melts: the importance of anionic polarization. *J. Phys.: Condens. Matter* **1993**, *5* (37), 6833−44.
(31) Kresse, G.; Furthmueller, J. Efficient iterative schemes for ab initio total-energy calculations using a plane-wave basis set. *Phys. Rev. B: Condens. Matter Mater. Phys.* **1996**, *54* (16), 11169−11186.
(32) Kresse, G.; Hafner, J. Ab initio molecular dynamics of liquid metals. *Phys. Rev. B: Condens. Matter Mater. Phys.* **1993**, *47* (1), 558−61.
(33) Bloechl, P. E. Projector augmented-wave method. *Phys. Rev. B: Condens. Matter Mater. Phys.* **1994**, *50* (24), 17953−79.
(34) Kresse, G.; Joubert, D. From ultrasoft pseudopotentials to the projector augmented-wave method. *Phys. Rev. B: Condens. Matter Mater. Phys.* **1999**, *59* (3), 1758−1775.
(35) Perdew, J. P.; Burke, K.; Ernzerhof, M. Generalized gradient approximation made simple. *Phys. Rev. Lett.* **1996**, *77* (18), 3865−3868.
(36) Le Roux, S.; Jund, P. Ring statistics analysis of topological networks: New approach and application to amorphous GeS2 and SiO2 systems. *Comput. Mater. Sci.* **2010**, *49* (1), 70−83.
(37) Yakel, H. L.; Brynestad, J. Refinement of the crystal structure of orthorhombic zinc chloride. *Inorg. Chem.* **1978**, *17* (11), 3294−6.
(38) Rundle, R. E.; Lewis, P. H. Electron-deficient compounds. VI. The structure of beryllium chloride. *J. Chem. Phys.* **1952**, *20*, 132−4.
(39) Dittmar, G.; Schaefer, H. Crystal structure of high-temperature germanium sulfide. *Acta Crystallogr., Sect. B: Struct. Crystallogr. Cryst. Chem.* **1975**, *31* (8), 2060−2064.
(40) Clark, S. J.; Segall, M. D.; Pickard, C. J.; Hasnip, P. J.; Probert, M. I. J.; Refson, K.; Payne, M. C. First principles methods using CASTEP. *Z. Kristallogr. - Cryst. Mater.* **2005**, *220* (5/6), 567−570.
(41) Refson, K.; Tulip, P. R.; Clark, S. J. Variational density-functional perturbation theory for dielectrics and lattice dynamics. *Phys. Rev. B: Condens. Matter Mater. Phys.* **2006**, *73* (15), 155114.
(42) Lee, M. H. Advanced pseudopotentials for large scale electronic structure calculations with application to a study of weakly ordered material - gamma-Al_2O_3. Ph.D. Thesis, Cambridge University, 1996.
(43) Sharma, B. K.; Wilson, M. Polyamorphism and the evolution of intermediate-range order in molten ZnCl2. *J. Phys.: Condens. Matter* **2008**, *20* (24), 244123.
(44) Bell, R. J.; Dean, P. Atomic vibrations in vitreous silica. *Discuss. Faraday Soc.* **1970**, *50*, 55−61.
(45) Galeener, F. L. Band limits and the vibrational spectra of tetrahedral glasses. *Phys. Rev. B: Condens. Matter Mater. Phys.* **1979**, *19* (8), 4292−7.
(46) Kinugawa, K.; Kadono, K.; Tanaka, H. Raman spectroscopic study on the structure of zinc chloride-zinc halide and zinc chloride-potassium halide (ZnCl2-ZnX2 and ZnCl2-KX (X = bromine, iodine)) glasses. *J. Non-Cryst. Solids* **1989**, *110* (2−3), 265−72.
(47) White, W. B.; DeAngelis, B. A. Interpretation of the vibrational spectra of spinels. *Spectrochim. Acta, Part A* **1967**, *23* (4), 985−95.
(48) Gupta, P. K.; Mauro, J. C. Composition dependence of glass transition temperature and fragility. I. A topological model incorporating temperature-dependent constraints. *J. Chem. Phys.* **2009**, *130*, 094503.
(49) Lucas, P. Mean coordination and topological constraints in chalcogenide network glasses. In *Chalcogenide glasses: Preparation, properties and applications*; Adam, J. L., Zhang, X. H., Eds.; Woodhead Publishing: 2014; pp 3−32.

DOI: 10.1021/acs.jpcb.6b02452
J. Phys. Chem. B XXXX, XXX, XXX−XXX